Plasma radicals as kinetics-controlling species during plasma-assisted catalytic NH_3 formation: support from microkinetic modeling

Tsung-Wei Liu[a], Fnu Gorky,[b] Maria L. Carreon,[b] Diego A. Gomez-Gualdron[a] *

[a] Department of Chemical and Biological Engineering, Colorado School of Mines, 1601 Illinois St, Golden CO, USA

[b] Department of Mechanical and Industrial Engineering, University of Massachusetts-Lowell, 1 University Ave, Lowell-MA, USA

*dgomezgualdron@mines.edu

ABSTRACT

About 1% of the world's CO_2 emissions are tied to the standard method to produce NH_3 (i.e., Haber-Bosch process), hence there is a need to decarbonize the production this chemical. To this end, plasma-assisted catalysis is emerging as a "green" alternative to synthesize NH_3. However, insufficient mechanistic understanding of this process has hindered significant improvements in its cost-effectiveness. Here we leverage "minimal plasma" microkinetic models and select experiments in a dielectric-barrier discharge (DBD) plasma reactor to look for missing mechanistic insights. Relatively robust to model assumptions, we find that our modeling supports the thesis that plasma N and H radicals are the kinetics-controlling plasma species for reactions involving the catalyst. This support stems from the realization that only the inclusion of N and H radicals in our models can readily explain key experimental observations for plasma-assisted NH_3 synthesis such as: *i)* similar catalytic activity for Fe and Ag (two metals at the opposite ends of N_2 dissociation capabilities), *ii)* activity increase in Fe (a metal that readily dissociates N_2) relative to thermal catalysis, and *iii)* detection of catalyst-bound N_2H_Y species. We also find the N radicals (a source of surface-bound N*) to be more important in nitrophobic metals and H radicals (a hydrogenating agent via Eley-Rideal reactions) to be more important in nitrophilic metals. On the other hand, other mechanistic aspects such as the kinetic relevance of N_2H_Y-forming pathways and dissolution reactions are discussed as a function of model assumptions. Our modeling suggests that some of these assumptions could be potentially clarified through *in situ* compositional analysis of catalyst adlayers (e.g., the fraction of radicals from the plasma bulk that reach the catalyst surface), as the adlayer composition seems to be rather sensitive to the plasma environment assumed to be "seen" by the catalyst.

KEYWORDS: *dielectric barrier discharge, minimal plasma, reaction mechanism, N_2Hy, Eley–Rideal reactions, sticking coefficient, subsurface dissolution,*

1. INTRODUCTION

NH_3 is the basis of fertilizers and is synthesized via the $N_2 + 3H_2 \leftrightarrow 2NH_3$ reaction, to the tune of over 200 million tons each year.[1] However, NH_3 synthesis is associated with ca. 1% of the world's CO_2 emissions.[2] As NH_3 will continue to be a critical chemical for the foreseeable future, a great challenge in the chemical industry is the decarbonization of NH_3 synthesis.[3] Currently, NH_3 is synthesized in high-pressure reactors (Haber-Bosch process), and in highly centralized fashion, largely overlapping centralized H_2 production.[4] The latter is responsible for most CO_2 emissions tied to NH_3 synthesis, as the H_2 feed comes from *in situ* CH_4 steam reforming ($CH_4 + H_2O \leftrightarrow 3H_2 + CO_2$) at the chemical plant.[2] Thus, the key to decarbonize NH_3 synthesis is to use "green" H_2 as feed instead.[5,6] But as green H_2 will be decentralized, decarbonized NH_3 synthesis will need decentralization as well. Such decentralization will need "quick response" reactors with fast turn-on/turn-off, given the likely intermittency of green H_2 (due its dependence on renewable electricity). The key issue is that quick-response reactors need to operate at mild conditions.

The HB process is harsh (i.e., pressures over 200 bar) to be able to circumvent equilibrium limitations imposed by the high temperature needed to thermocatalytically dissociate N_2 at acceptable rates. Thus, one alternative to achieve NH_3 synthesis at mild conditions (i.e., low pressure) is to couple the catalyst to a plasma.[7] As envisioned, renewable electricity would be used to create a non-thermal plasma that would ultimately facilitate the appearance of catalyst-bound N* (the species whose hydrogenation leads to NH_3) at lower temperatures than in the thermocatalytic process.[3] Although numerous reactions occur in the plasma phase, the key to facilitate the appearance of N* is thought to be the collision of gas-phase N_2 with "hot" electrons, which would "pre-activate" N_2 before it reaches the catalyst. Depending on the energy of the colliding electron, the pre-activation could consist of either converting N_2 into a vibrationally excited species ($N_2(v)$, where v is the vibrational level, $v = 0, 1, \ldots$) or directly dissociating N_2 into two N radicals.

Currently, the highest ammonia energy yield reported for catalytic, plasma-assisted NH_3 synthesis is 36 g_{NH3}/kWh,[8] in contrast to the 100 to 200 g_{NH3}/kWh some estimate as needed for economic feasibility of decentralized NH_3 production.[8,9] Thus, a 3- to 6-fold improvement is needed, but one obstacle hindering fast and rational improvement of energy yields in plasma reactors is the insufficient mechanistic understanding of how NH_3 forms in the joint presence of a plasma and a catalyst. Mechanistic aspects of plasma-assisted NH_3 synthesis that seem to be approaching a consensus are: *i)* the non-Arrhenius dependence of NH_3 formation rates with temperature,[10,11] *ii)* the ability to reach conversions beyond thermal equilibrium,[9,12] *iii)* the first order dependence of NH_3 formation rates on N_2 pressure,[10] *iv)* the relative compositional similarity of the bulk

plasma phase for experiments with different (metal) catalysts,[3] and *v)* the presence N and H atomic species in the plasma (along with $N_2(v)$ and other species).[13–16]

But other mechanistic aspects that remain under debate include *i)* whether the NH_3 formed on the catalyst comes primarily from pathways involving $N_2(v)$ or from those involving N radicals. Namely, it remains unclear whether the kinetically controlling species is $N_2(v)$ or N radicals (or some other). Note that resolution to this specific mechanistic aspect could shed light on the maximum achievable ammonia energy yields for the plasma-assisted process and/or inform strategies for plasma generation. *ii)* whether alternative pathways such as those involving N_2H_Y species (whose detection during plasma-assisted NH_3 synthesis has been reported in some works)[13,15,17] present any kinetic relevance, *iii)* whether hypothesized effects such as the "hydrogen sink" effect[18]—where H dissolution protects the loss of catalyst-bound H* species (needed for hydrogenation steps), and *iv)* whether the dominant reaction pathway (and thus the answer to mechanistic questions) changes with catalyst composition.

As collected information about the identity and concentration of species in the plasma bulk is not necessarily reflective of what the catalyst surface "sees." The major obstacle in addressing the mechanistic questions above is the exceptional difficulty in characterizing the plasma-catalyst interface under operando conditions. Thus, clever reactor setups and experiments need to be designed to indirectly infer mechanistic aspects.[9,13,19–22] For instance, from mass balances and measurements in reactors of various lengths with plasma jets characterized by molecular beam mass spectroscopy (MBMS), Bruggeman and co-workers recently obtained evidence suggesting that $N_2(v)$ did not contribute towards NH_3 formation, suggesting N and H radicals to be involved.[23]

Given the experimental characterization challenges, computational modeling has been used as a complementary tool, aiming to provide insights that could explain experimental observables. Some computational efforts include zero-dimensional reactor models that consider numerous reactions in the plasma bulk (and thus an evolving plasma phase), while including some reactions that involve the catalyst.[16,24–26] Along with experimental bulk plasma characterization, these models have helped shed light on the complex behavior of the plasma phase.[14,26] However, they have been arguably more uncertain in their description of reactions involving the catalyst. For instance, the "efficacy" with which plasma species reach and react on the catalyst is accounted for by empirically fitted sticking coefficients.[26,27] But usually there are numerous other parameters empirically fitted as well, creating the possibility of non-unique solutions, hence uncertainty about the physical meaningfulness of these parameters and the insights obtained therein. For instance, consider that parameter fitting sometimes have yielded reaction parameters inconsistent with density functional theory (DFT).[14,16,27]

Accordingly, an emerging goal in plasma-assisted catalysis is the implementation of DFT-informed microkinetic modeling approaches that have proven useful in thermal catalysis.[14,24,28,29] In thermal catalysis, microkinetic modeling have shed light on reaction mechanisms and proven useful to capture activity (and selectivity) trends across different catalysts, making it a powerful tool for catalyst screening.[30,31] For the latter purpose, models tend to assume that the catalyst surface "sees" a constant reactant concentration (echoing differential reactor conditions), and that this concentration is equal to the reactant concentration in the bulk fluid phase. Translation of this approach to plasma catalysis requires to bypass modeling of the plasma itself and assume that the catalyst faces a constant "minimal" plasma phase that only features the *key* species ultimately "seen" by the catalyst, at the concentrations "seen" by the catalyst in the actual system. These concept has been formally used before by Schneider and coworkers.[3,12,29] But as the mechanism of plasma-assisted NH_3 synthesis is not well understood, it is unclear which species and/or reactions are important and should appear in such minimal plasma.

The work herein, however, is based on the alternative view that one can exploit the simplicity of the minimal plasma to decouple the effect of different species (and concentrations) and reactions and understand their impact on NH_3 production rates and mechanisms. Moreover, one could infer which species (at what concentration) the catalyst "sees" (and their importance) by identifying the minimal plasma composition (and reactions that need to be included in the model) to capture experimental trends across different metals. To be sure, this exercise assumes relative similarity of the plasma when different catalysts are used, but such assumption is supported by earlier optical emission spectroscopic (OES) measurements by us—at least for Fe, Ni, Co, Pd, Cu, Ag, and Au. In principle, once what the catalyst "sees" is established, the corresponding reaction mechanisms could be studied in detail from modeling.[3]

For a brief recount on the use of DFT-informed microkinetic models to study plasma-assisted NH_3 system, notice that Mehta *et al.*[14] used microkinetic modelling, with the minimal plasma including N_2, H_2 and vibrationally excited $N_2(v)$ to explain *i)* the higher NH_3 production activity of Co compared to Fe, Ru, Ni and Pt at 438 K and 1 bar, and *ii)* overall increase in NH_3 production rates across all these metals relative to the thermal catalysis. The omission of N radicals was rationalized by the expected higher abundance of $N_2(v)$ compared to N radicals due to the expected energy distribution of electrons (whose collision with N_2 generates either $N_2(v)$ or N•). However, the reactivity of plasma radicals could mean that, even at notably smaller concentrations, radicals could have an impact on NH_3 formation. For instance, in our recent DFT work,[3] enthalpic barriers for Eley-Rideal (ER) reactions for N and H radicals with surface-bound species seemed inexistent regardless of the apparent difficulty (geometry-wise) of the reaction. More recently, Engelman *et al.* [24] proposed microkinetic modelling including ER reactions with N and H radicals, illustrating that these radicals can also increase NH_3 production rates relative to thermal catalysis. These authors focused on the effect of entropic assumptions on modeling results, while keeping the minimal plasma composition constant, and not including reactions that could form N_2Hy species.

As noted earlier, N_2Hy is an intriguing species that have been detected via FTIR and/or MBMS measurements during some plasma-assisted NH_3 synthesis experiments. The presence of this species may suggest the operation of reaction pathways alternative to the established HB ones and may provide an

additional reference for comparison between modeling and experiments. Based on all the above, herein we specifically used DFT-informed microkinetic modeling to study NH_3 formation under a minimal plasma containing different concentrations of N_2, H_2, $N_2(v)$, $H_2(v)$, as well as N and H radicals. For the first time, we considered reactions that could form N_2H_Y species as well as dissolve N and H into the catalyst subsurface. We studied these reactions on seven transition metals (Fe, Ni, Co, Pd, Cu, Ag, Au), focusing on interrogating the previously mentioned mechanistic aspects under debate—with emphasis on the plausibility of plasma radicals as kinetics-controlling species—and trends across metals. Previously reported data by us[3] was leveraged to initially guide the discussion of our results, while select new experiments on a dielectric barrier discharge (DBD) plasma-reactors were performed as needed to further enhance comparison between modeling and experiments.

2. COMPUTATIONAL METHODS

Baseline microkinetic model. A "baseline" microkinetic model was built relative to which changes in minimal plasma composition, sticking coefficients for Eley-Rideal (ER) reactions involving plasma radicals, entropy assumptions, and reactions included/excluded were made. To build the model, mass balances for all potential surface species "*i*" were made. All species of the form N_XH_Y were considered with *x* and *y* each varying from 0 to 2, and 0 to 6, respectively. The generic mass balance for species *i* is described by Eq. 1:

$$\frac{\partial \theta_i}{\partial t} = \sum_j^m c_{i,j}\ r_j \qquad (1)$$

where θ_i is the fractional coverage of species *i* on the catalyst surface, $c_{i,j}$ is the stoichiometric coefficient of species *i* in reaction *j* and r_j is the corresponding reaction rate. The reaction rate is described by Eq. 2:

$$r_j = k_{f,j} \prod_{f,j} a_{f,j}^{c_{i,j}} - k_{b,j} \prod_{b,j} a_{b,j}^{c_{i,j}} \qquad (2)$$

where $k_{f,j}$ and $k_{b,j}$ are the rate constants of forward and backward reaction, and $a_{f,j}$ and $a_{b,j}$ are either fractional coverage (if species is a surface-bound species) or partial pressure (if species is a gas species) for reactants and products, respectively in reaction *j*. The balance of surface sites provides a constraint to the model according to Eq. 3:

$$1 = \sum_i^n \theta_i + \theta^* \ (3)$$

The rate constants in Eq. 2 are calculated using the Eyring equation:

$$k = \frac{k_B T}{h}\ e^{\frac{-\Delta H^{\neq}}{RT}}\ e^{\frac{\Delta S^{\neq}}{R}} \qquad (4)$$

where the k_B, h, R, and T are the Boltzmann constant, Planck constant, idea gas constant, and temperature, respectively. On the other hand, $\Delta H^{\neq}$ and $\Delta S^{\neq}$ are the enthalpic and entropic barriers separating reactants and products. All the reactions are assumed to occur on the closed-packed facets of the studied metals, which in an assumption justified by the work of Schneider and coworkers.[14] The values for $\Delta H^{\neq}$ were taken from our previous work,[3] in which these barriers were obtained from DFT calculations and/or DFT-derived scaling relationships relating the enthalpic barriers to reaction energies. Scaling relationships for N_2H_Y dissociation barriers were derived by ourselves in earlier work,[3] those for Langmuir-Hinshelwood (LH) hydrogenation barriers were obtained from work by Nørskov and coworkers,[32] while those for adsorptive dissociation barriers were obtained from Vojvodic and coworkers.[33] Reaction energies used as input for the scaling relationships were calculated by us in earlier work.[3] Consistent with our earlier DFT calculations, enthalpic barriers for all ER and radical adsorption reactions were set to zero. All barriers and reaction energies are freely available in tabulated form as supplemental information in ref.[3] . In the above cited works, all DFT calculations were done with either the RPBE or PBE functional.

As for the values for $\Delta S^{\neq}$, two different assumptions were made For reactions involving two surfaces species (i.e., LH reactions), $\Delta S^{\neq}$ was assumed to be zero as justified in our previous work.[3] For reactions involving one surface species and one gas species *l* (i.e., ER reactions), or adsorption of a gas species *l*, we considered a "minimal entropy loss" scenario where at the transition state the gas species loses *at least* one third of its original entropy ($\Delta S^{\neq}$ = 1/3 $S_{l\text{-gas}}$). Briefly, one can infer that at least one third of entropy is lost because in consistency with transition state theory, a transition state has one less degree of freedom than the reactant states. For thermodynamic consistency, $\Delta S^{\neq}$ = 2/3 $S_{l\text{-gas}}$ for reactions involving the desorption of species *l*. To calculate $S_{l\text{-gas}}$, thermochemical tables from NIST were used to first calculate $S^o_{l\text{-gas}}$, followed by temperature adjustment according to Eq. 5:

$$S = A\ln(\tau) + B\tau + C\frac{\tau^2}{2} + D\frac{\tau^3}{3} - \frac{E}{2\tau^2} + G \quad (5)$$

where τ is the absolute temperature T divided by one thousand. Subsequent adjustment for both temperature and pressure was made according to:

$$S = R + R\ln\big(q(V,T)\big) + RT\left(\frac{\partial lnq}{\partial T}\right) \qquad (6)$$

where q is the partition function.

The "minimal plasma" consisted of N_2, $N_2(v)$, H_2, $H_2(v)$, N• and H• species at a total pressure of 1 bar and a temperature of 400 K to mimic experiments in atmospheric DBD reactors, such as those performed and presented in our previous work.[3] The minimal plasma *baseline* composition was taken from plasma modeling by Bogaerts and coworkers.[25] These authors found that for a N_2:H_2 mixture at 3:1 ratio at a total pressure of 1 bar, the partial pressures of N and H radicals at the plasma uniform region were predicted to be $1.9\text{x}10^{-4}$ bar and $1.5\text{x}10^{-2}$ bar, respectively. The partial pressures of $N_2(v)$ and $H_2(v)$ were calculated using the Treanor and Boltzmann distribution, respectively, with a vibrational temperature T_{vib} equal to 3000 K. The equations for both distributions can be found in the SI,

along with the resulting distribution of vibrationally excited species for T_{vib} = 3000 (**Table S1**).

Table 1. Comprehensive list of reactions considered in baseline microkinetic model.

One-step gas dissociation	ER nitrogenation	LH N_2H_x hydrogenation	N_2Hx dissociation
r_1: $N_{2(g)} + 2^* \longrightarrow 2N^*$	r_{16}: $N_{(g)} + H^* \longrightarrow NH^*$	r_{31}: $N_2^* + H^* \longrightarrow N\text{-}NH^* + *$	r_{43}: $NNH^* + * \longrightarrow N^* + NH^*$
r_2: $H_{2(g)} + 2^* \longrightarrow 2H^*$	r_{17}: $NH^* + N_{(g)} \longrightarrow N\text{-}NH^*$	r_{32}: $NNH^* + H^* \longrightarrow N\text{-}NH_2^* + *$	r_{44}: $NNH_2^* + * \longrightarrow N^* + NH_2^*$
Two-step gas dissociation	r_{18}: $NH_2^* + N_{(g)} \longrightarrow N\text{-}NH_2^*$	r_{33}: $NNH^* + H^* \longrightarrow HN\text{-}NH^* + *$	r_{45}: $NNH_3^* + * \longrightarrow N^* + NH_3^*$
r_3: $N_{2(g)} + * \longrightarrow N_2^*$	**ER N_2H_x hydrogenation**	r_{34}: $NNH_2^* + H^* \longrightarrow N\text{-}NH_3 + *$	r_{46}: $HNNH^* + * \longrightarrow 2NH^*$
r_4: $H_{2(g)} + * \longrightarrow H_2^*$	r_{19}: $N_2^* + H_{(g)} \longrightarrow N\text{-}NH^*$	r_{35}: $NNH_2^* + H^* \longrightarrow HN\text{-}NH_2^* + *$	r_{47}: $H_2NNH_2^* + * \longrightarrow 2NH_2^*$
r_5: $N_2^* + * \longrightarrow 2N^*$	r_{20}: $NNH^* + H_{(g)} \longrightarrow N\text{-}NH_2^*$	r_{36}: $HNNH^* + H^* \longrightarrow HN\text{-}NH_2^* + *$	r_{48}: $HNNH_3^* + * \longrightarrow NH^* + NH_3^*$
r_6: $H_2^* + * \longrightarrow 2H^*$	r_{21}: $NNH^* + H_{(g)} \longrightarrow HN\text{-}NH^*$	r_{37}: $NNH_3^* + H^* \longrightarrow HN\text{-}NH_3^* + *$	r_{49}: $H_2NNH_3^* + * \text{ --> } NH_2^* + NH_3^*$
LH NH_x hydrogenation	r_{22}: $NNH_2^* + H_{(g)} \longrightarrow N\text{-}NH_3^*$	r_{38}: $HNNH_2^* + H^* \longrightarrow HN\text{-}NH_3^* + *$	**N_2Hx desorption**
r_7: $N^* + H^* \longrightarrow NH^* + *$	r_{23}: $NNH_2^* + H_{(g)} \longrightarrow HN\text{-}NH_2^*$	r_{39}: $HNNH_2^* + H^* \longrightarrow H_2N\text{-}NH_2^* + *$	r_{50}: $HNNH^* \longrightarrow HNNH_{(g)} + *$
r_8: $NH^* + H^* \longrightarrow NH_2^* + *$	r_{24}: $NNH_3^* + H_{(g)} \longrightarrow HNNH_3^*$	r_{40}: $HNNH_3^* + H^* \longrightarrow H_2N\text{-}NH_3^* + *$	r_{51}: $H_2NNH_2^* \longrightarrow H_2NNH_{2(g)} + *$
r_9: $NH_2^* + H^* \longrightarrow NH_3^* + *$	r_{25}:$HNNH^* + H_{(g)} \longrightarrow HN\text{-}NH_2^*$	r_{41}: $H_2NNH_2^* + H^* \longrightarrow H_2N\text{-}NH_3^* + *$	r_{52}: $NNH^* \longrightarrow NNH_{(g)} + *$
NHx desorption	r_{26}: $HNNH_2^* + H_{(g)} \longrightarrow HN\text{-}NH_3^*$	r_{42}: $H_2NNH_3^* + H^* \longrightarrow 2NH_3^*$	**ER recombination**
r_{10}: $NH_3^* \longrightarrow NH_{3(g)} + *$	r_{27}: $HNNH_2^* + H_{(g)} \longrightarrow H_2N\text{-}NH_2^*$		r_{53}: $N_{(g)} + N^* \longrightarrow N_2^*$
Radical Adsorption	r_{28}: $H_2NNH_2^* + H_{(g)} \longrightarrow H_2N\text{-}NH_3^*$		r_{54}: $H_{(g)} + H^* \longrightarrow H_2^*$
r_{11}: $N_{(g)} + * \longrightarrow N^*$	r_{29}: $HNNH_3^* + H_{(g)} \longrightarrow H_2N\text{-}NH_3^*$		
r_{12}: $H_{(g)} + * \longrightarrow H^*$	r_{30}: $H_2NNH_3^* + H_{(g)} \longrightarrow 2NH_3^*$		
ER NH_x hydrogenation			
r_{13}: $H_{(g)} + N^* \longrightarrow NH^*$			
r_{14}: $H_{(g)} + NH^* \longrightarrow NH_2^*$			
r_{15}: $H_{(g)} + NH_2^* \longrightarrow NH_3^*$			

Analogous to N_2 and H_2, $N_2(v)$ and $H_2(v)$ can undergo dissociative adsorption, but with an enthalpic barrier reduced by an amount consistent with the vibrational excitation, in the spirit of the "alpha" model" used by Mehta et al.[14] Here:

$$E_a^{'} = E_a - nE_v \qquad (7)$$

where E_a' is the reduced dissociation barrier for the vibrationally excited species, E_a is the dissociation barrier for the ground state species, E_v is one quantum of vibrational energy (0.29 eV for $N_2(v)$ and 0.56 eV for $H_2(v)$). For instance, for $N_2(v = 1)$ dissociation in Ag, the barrier is reduced by 0.29 eV from 6.65 eV to 6.36 eV. Whereas for $N_2(v = 2)$ the barrier would be further reduced to 6.07 eV.

The microkinetic model was built in Python-3.9.13 leveraging the `scipy.integrate.solve_ivp` library, with the `radau` or `BDF` methods called when the model yielded a systems of ordinary differential equations (ODEs) that were stiff in nature. The systems of ODEs were numerically solved to yield the evolution of θ_i with time until a steady state is reached where all $\frac{\partial \theta_i}{\partial t}$ are equal to zero (within a $1x10^{-10}$ tolerance). At that point, the steady state values of θ_i were used to calculate turnover frequencies (TOFs). The reactions considered in the model are listed in **Table 1**

3. EXPERIMENTAL METHODS

Dielectric barrier discharge reactor. Different metal electrodes were also assessed in an *in-house* built atmospheric DBD reactor, whose setup has been described in detail in previous work[4-6] and schematized in Fig. S1. For the catalytic tests in this reactor, N_2 and H_2 cylinders, were connected to the reactor using mass flow controllers. The reactions were carried out at 25 sccm of total flow rate with an equimolar feed ratio of nitrogen to hydrogen (3:1) (N_2:H_2). The plasma power varied from 5-20 Watts with 25 ± 0.8 kHz frequency. All the metal electrodes employed in this study had 2.0 mm diameter and 152 mm length (**Table S2**). Alfa-Aesar, 99.995% Ni, Ag, and Fe metal basis wires were employed as electrodes. Wire from Midwest Tungsten Service was employed as W electrode. The outer electrode was made of tinned copper mesh acting as the ground electrode. The electrical characterization was carried out by measuring the applied voltage to the reactor by employing a high-voltage probe (Tektronix P6015A). The charge was calculated using the voltage measurement across a capacitor. The two probes were connected to an oscilloscope (Tektronix TDS2014C). The capacitor was connected to the reactor in series with the ground electrode. The high-voltage power supply was connected to the reactor using a litz wire and alligator clips. The inner electrodes were placed at the centre of the quartz tube with an ID of 4 mm and an OD of 6.35 mm.

Gas Chromatography. The gases collected from the reactor exit were sent to an online gas chromatograph to determine the ammonia synthesis rate. The quantification was performed using an Agilent 8860A GC with an HP-PLOT U column (30 m × 0.320 mm × 10 μm) and hydrogen as the carrier gas.

Optical Emission Spectroscopy. The light emitted from the discharge was led through an optical system, and the emission spectra of the glow region were measured at three different locations of the tube (before the reaction center, at the reaction center, and after the reaction center) for a comprehensive understanding on the difference of plasma species. The measurements were recorded using a dual-channel UV-VIS-NIR spectrophotometer in scope mode (Avantes Inc., USB2000 Series). The spectral range was from 200-1100 nm, using a line grating of 600 lines/mm and a resolution of 0.4 nm. A bifurcated fibre optic cable with 400 µm was employed. For accuracy, integration time was set at 5 seconds with 100 averaging.

4. RESULTS AND DISCUSSION

4.1. Support for kinetic relevance of N and H radicals

N radicals vs. $N_2(v)$ on the generation of N*. The original vision for plasma-assisted catalytic NH_3 synthesis was to facilitate the generation of N* at low enough temperatures so that high pressure—to shift the equilibrium conversion limit—was not necessary. In principle, N* generation can be facilitated by the formation of both $N_2(v)$ and N radicals in the plasma. $N_2(v)$ can be formed upon N_2 collision with electrons contain energy above 0.3 eV, while N formation requires electrons around 9.5 eV in energy. Given the shape of the electron energy distribution functions (EEDF) at typical electron temperatures in a DBD reactor (e.g., 1 eV), where electrons at least 9.5 eV in energy are orders of magnitude less abundant than electrons at least 0.3 eV in energy[26,34] $N_2(v)$ is expected to be orders or magnitude more abundant in the plasma bulk than N radicals. Moreover, plasma modeling by Bogaerts and coworkers[25] supports the above to be the case. In earlier work, we predicted the adsorption energetics of $N_2(v)$ and $N_{2(g)}$ adsorption (*r1*) to be similar,[3] but N* formation from dissociation (*r1* or *r5*) is expected to be easier for the vibrationally excited species. Mehta et al.[14] proposed the dissociation enthalpic barrier for $N_2(v)$ to be effectively reduced (relative to $N_{2(g)}$) by an amount equal to the vibrational excitation energy. However, while N radicals could be orders of magnitude less abundant than $N_2(v)$, the adsorption of N radicals (*r11*) can generate N* without an enthalpic barrier.

To examine the competition between $N_2(v)$ and N radicals to generate N*, we truncated the baseline microkinetic model (see baseline assumptions in methods) to include only reactions *r1*, *r3*, and *r5*. We evaluated the rates for N* formation (**Fig. 1**) at 400 K and a 3:1 N_2/H_2 feed at 1 bar to facilitate the use of our DBD experiments performed herein as a point of reference for discussion. To facilitate discussion, we use partial pressure as a surrogate for concentration, and we assume this partial pressure to correspond to what the catalyst "sees" at the plasma-catalyst interface. The partial pressure of each kind of $N_2(v)$ species was calculated with the Treanor distribution, assuming a 3000 K vibrational temperature and truncating the distribution at the 10th level of vibrational excitation (i.e., $v = 1$, 2… 10). For a detailed breakdown of the vibrationally excited population, see **Table S1**). The partial pressure of N radicals was modulated from 0.2 x 10^{-49} bar to 0.2 bar to consider different competition scenarios. For the highly nitrophilic Fe, we found that a partial pressure of N radicals equal to ~0.1 bar was needed for N radicals to outcompete $N_2(v)$ as an N* source. On the other hand, for the highly nitrophobic Au, we found that just a partial pressure of N radicals equal to ~0.6 x 10^{-49} was needed to for N radicals to outcompete $N_2(v)$ as an N* source.

Considering that previous plasma models by Engelmann et al [24] on DBD reactors at similar conditions as discussed here predicted N radical concentrations around 0.1 x 10^{-3} bar, one can infer that: *i)* For the highly nitrophilic Fe, even if all N radicals generated in the plasma bulk make it to the catalyst surface, N radicals could not outcompete $N_2(v)$ as an N* source, *ii)* For the highly nitrophobic Au (or Ag), even if only a 10^{-45} fraction of all N radicals generated in the plasma bulk make to the catalyst surface, N radicals would be the primary source of N*. The above is consistent with the dramatic

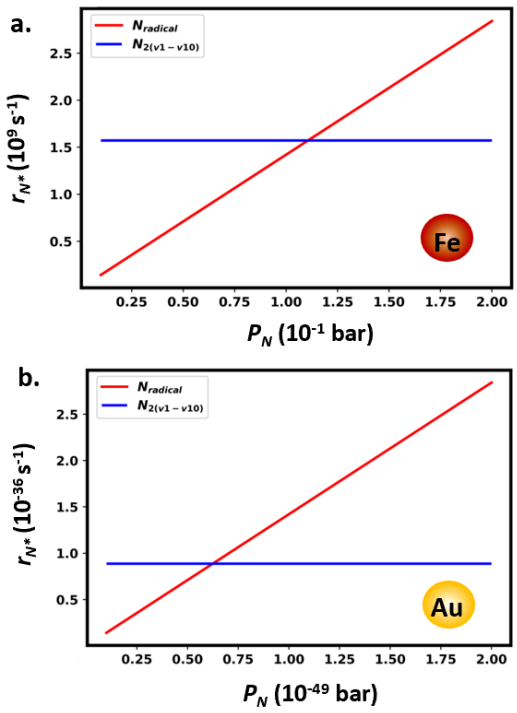

Fig. 1. Comparison of N* rates of formation on clean catalyst surfaces from two parallel routes for different N radical partial pressures. From dissociative adsorption of $N_2(v)$ (r_1) (blue line) and from N radical adsorption (r_{11}, red line). Rates are calculated at 400 K and a gas phase at 1 bar total pressure primarily consisting of a 3:1 N_2:H_2 mixture. $N_2(v)$ partial pressures are calculated with the Treanor distribution assuming a 3000 K vibrational temperature. Top: nitrophilic metal (Fe). Bottom: nitrophobic metal (Au or Ag).

differences in enthalpic barriers for N_2 dissociation between Fe and Au (or Ag). In Fe this barrier is very low, already being zero for $N_{2(g)}$ *r1*). In Au (or Ag) this barrier is very high (~6.3 eV), even staying at ~3.3 eV for *r1* for $N_2(v=10)$. Accordingly, at least in nitrophobic metals, N radicals must be the source of N*. Note that different variations of the assumptions of the

truncated microkinetic model (while not discussed here) do not alter the latter observation. Moreover, considering that in plasma-assisted NH_3 synthesis in DBD reactors, Au (or Ag) performs *at least* as well as Fe, one suspects that a significant fraction of N radicals must make it to the catalyst surface.

N radicals vs. $N_2(v)$ on the generation of N* on the relative performance across metals. One consistent experimental observation reported elsewhere (and confirmed once again here) is that catalysts that were inactive for thermocatalytic NH_3 synthesis present significant activity for plasma-assisted NH_3 synthesis.[3,18,35] Moreover, while in thermocatalytic NH_3 synthesis experiments one can observe differences in activity across catalysts spanning more than twenty orders of magnitudes, in the plasma-assisted case, widely different catalysts are found to perform much closer together. Based on the similarity of the OES spectra collected in DBD experiments (**Table S5**), one can reasonably assume that, for the catalysts studied here, the contribution of "just plasma" reactions to NH_3 production is relatively similar (at least in

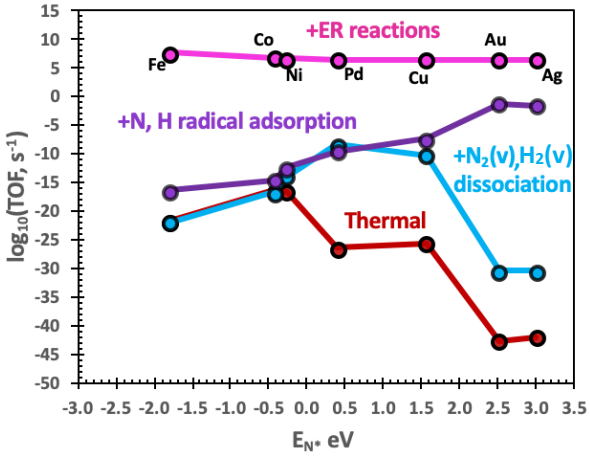

Fig. 2. Calculated turnover frequencies (TOFs) for NH_3 production on different metals, with different reactions turned on/off on the baseline microkinetic model. Red: only standard reactions for thermal catalysis are on. Blue: dissociation reactions for $N_2(v)$ added to the "red" model. Purple: N and H radical adsorption reactions added to the "blue" model. Pink: ER reactions added to the "purple" model. TOFs are calculated at 400 K and a gas phase at 1 bar total pressure primarily consisting of a 3:1 N_2:H_2 mixture. $N_2(v)$ partial pressures are calculated with the Treanor distribution assuming a 3000 K vibrational temperature, partial pressures of N and H radicals are 1.9×10^{-4} bar and 1.5×10^{-2} bar, respectively.

terms of orders of magnitude). Thus, differences in TOF_{NH3} values across metals must primarily originate from reactions involving the catalyst. Accordingly, to assess what kind of "catalyst" reactions must occur to have relative catalyst performance aligned with experimental observations, we ran the baseline microkinetic model with different reactions turned on and off (**Fig. 2**). The minimal plasma conditions for **Fig. 2** are the same as for **Fig. 1**, only that now the partial pressures of N and H radicals were fixed at 1.9×10^{-4} bar and 1.5×10^{-2} bar, respectively.

When only the reactions relevant to thermal catalysis are included (*r1-r10* and *r31-r52*), our model reveals a volcano plot with orders of magnitude differences between metals such as Fe, Ni, Cu and Au (red model, **Fig. 2**), but, overall, one can consider all TOF_{NH3} values to be negligible (below 10^{-15} s^{-1}). The latter prediction is consistent with experiments running the DBD reactor with the plasma off, where no NH_3 was detected leaving the reactor. Once, $N_2(v)$ and $H_2(v)$ are brought into the picture as a source of N* and H* (via dissociation reactions *r1* and *r2*), the top of the volcano plot is predicted to shift (a similar trend to that reported by Mehta *et al.*[14] in earlier models that also only added $N_2(v)$ dissociation reactions to the thermal case), in our case with Pd at the top instead of Ni. However, when only $N_2(v)$ and $H_2(v)$ are added to the thermal model, orders of magnitude differences in TOFs across catalysts remain (see blue line in **Fig. 2**). Thus, the similar performances for different catalysts in plasma-assisted NH_3 synthesis cannot be readily explained by the dissociation of $N_2(v)$ and $H_2(v)$.

The addition of N and H radical adsorption reactions (*r11-r12*) continues to shift the top of the volcano plot towards the most nitrophobic metals (see purple line **Fig. 2**), with orders of magnitude differences in TOFs across different metals remaining. In this scenario, a metal such as Au, which is inactive in thermocatalytic NH_3 synthesis, is predicted to be orders of magnitude more active than "traditional" ammonia catalysts such as Fe and Ni in consistency with *i)* N and H radical adsorption (*r11-r12*) dramatically boosting the availability of N* and H* in Au but not so in Fe and Ni (e.g., recall the enthalpic barrier for *r1* in Fe is already zero in the thermal case), and *ii)* the lower calculated barriers for Langmuir-Hinshelwood hydrogenation reactions (*r7-r9*) in Au relative to in Fe and Ni. Only when ER reactions (*r13-r30 and r53-54*) are added to the model (most of which are hydrogenation reactions involving the collision of H radicals with surface-bound species), performance across different metals come within similar orders of magnitude (see pink line in **Fig. 2**). Thus, the joint inclusion of adsorption and ER reactions involving radicals brings model predictions dramatically closer to experimental rate trends across metals than the inclusion of dissociation reactions for vibrationally excited species can. Data for the models in **Fig. 2** can be found in tabulated form in **Table S3**.

N radicals vs. $N_2(v)$ on the boost of NH_3 production relative to thermal catalysis. As a point of comparison with experimental trends, another interesting prediction is that $N_2(v)$ dissociation reactions on their own are not capable of boosting the performance of Fe relative to the thermal case. To a lesser extent, this is also true for Ni and Co, where $N_2(v)$ dissociation somewhat boosts activity relative to the thermal case, but arguably not enough for the overall performance to be "non-negligible" in practical terms. In fact, while $N_2(v)$ dissociation does boost activity for a metal such as Ag (or Au) by about ten orders of magnitude relative to the thermal case, the boosted activity is still too small to be considered "non-negligible".

With these observations in mind, we considered meritorious to experimentally compare the ammonia formation rates in the presence of Fe, Ni and Ag for the thermal and plasma cases (in a DBD reactor) (**Fig. 3**).

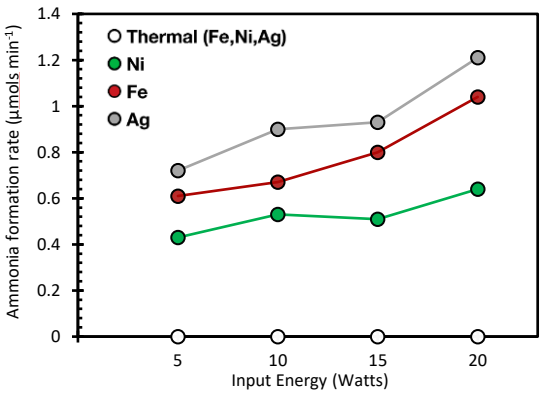

Fig. 3. Comparison between estimated *minimum* "catalyst-only" NH_3 formation rate for plasma-assisted cases (at different powers) and the thermal case. All experiments were done at 400 K and a gas phase at 1 bar total pressure, with a feed consisting of a 3:1 N_2:H_2 mixture. The thermal condition did not produce any detectable ammonia with any metal. It was assumed that the NH_3 formation rate for plasma-assisted W case would be the *maximum* contribution that plasma would have to NH_3 formation across all metals.

Consistent with predicted TOF_{NH3} values below 10^{-15} s^{-1}, experiments with Fe, Ni and Au did not result in NH_3 detection when the plasma was off (i.e., reaction rate was negligible). On the other hand, when the plasma power was on, NH_3 was detected (i.e., reaction rate was significant). For instance, even at the lowest power tested herein (5 W), the estimated NH_3 formation rates for Fe, Ni and Ag ranged between 0.56 and 0.85 μmol min^{-1}. To be sure, these rates include the contribution of plasma reactions to NH_3 production. Thus, while it is challenging to decouple catalyst and plasma contributions, we attempt to estimate a *reasonable* range for the latter, so that it can be subtracted to experimental rates.

To do so, we first direct our attention to the experiments with W. OES measurements for the W system and the studied metals are within the same order of magnitude. Although OES cannot be used to quantitatively determine the concentration of specific plasma species, the overall similarity of OES (denoted by similar intensities for key emission peaks) across metals, can be used as a reasonable indication of plasma composition similarity, and thus comparable contribution of the plasma to NH_3 production for the W case relative to the Fe, Ni and Ag ones (**Table S5**). Two extreme scenarios can be considered for the W case: either all NH_3 is being produced from the plasma (maximum contribution scenario, 0.13 μmol min^{-1}) or all NH_3 is being produced from the catalyst (minimum contribution scenario, 0.00 μmol min^{-1}). Thus, subtracting the above rate contribution range from the measured reaction rates for Fe, Ni and Ag cases generates a plausible interval for catalyst contribution to NH_3 production for the latter three cases. The "uncertainty" intervals for the "catalyst contribution" are presented in **Fig. S4** for these metals, with the lower-bound of the intervals corresponding to the data presented in **Fig. 3**. From this exercise, one can see that, for the three metals, catalyst contribution to NH_3 production is dramatically larger than for the thermal case. Again, this experimentally observed scenario cannot be explained without considering N and H radicals reaching the catalyst surface. But note that to explain enhanced performance, it is not enough to just consider N and H radicals as a source of N* and H*. From the Fe and Ni cases, one can see that ER reactions must be also considered to explain boosts that are experimentally detectable.

To be sure, the predicted TOF (and thus rate) boosts are arguably excessively large (TOF_{NH3} values larger than 10^6 s^{-1}) when considering that all N and H radicals in the plasma bulk reach the catalyst surface *and* that reactions (adsorption) always occurs when these radicals reach a surface-bound species (free active site). However, the lifetime of radicals in the gas phase depends on their density, and radical-radical reactions are often dominant losses. This situation suggests that only a fraction of plasma bulk radicals reach the surface and/or that reactions on the catalyst involving collisions with radicals are not always effective (even if sufficient energy is carried by the radical to overcome any potential barrier). We examine this in detail in the following subsection.

On the extent N radicals may reach the catalyst surface and react. In **Fig. 4a**, one can see a comparison across metals based on predicted TOF_{NH3} values for different fractions of bulk radicals reaching the catalyst, as given by the parameter ρ. Specifically, ρ is the ratio between a "trial" partial pressure of N and H radicals immediately above the catalyst surface and the partial pressure of these radicals in the bulk (1.9×10^{-4} bar and 1.5×10^{-2} bar, respectively). The reactivity of plasma radicals generated in the plasma bulk, implies that only a small fraction of these species makes it to the catalyst before reacting with other species. However, **Fig. 4a** shows that, at 400 K and a 3:1 N_2:H_2 mixture at 1 bar as feed, just around one hundred thousandth of the generated N and H radicals need to reach the catalyst for all the metals to facilitate similar TOFs. As the experimental observation *is* that metals perform similarly, this observation from the model arguably place an *approximate lower bound* to the extent that N and H radicals reach the surface.

The TOF trends in **Fig. 4b**, which is analogous to **Fig. 4a** but with ER reactions turned off (by setting the sticking coefficient S_{0ER} to zero), shows that the participation of N and H radicals is not limited to providing N* and H* species (*r11-r12*) as precursors for LH reactions. In the scenarios presented in **Fig. 4b**, there is no value of ρ where metals would all have TOFs (and thus rates) within similar orders of magnitude as observed experimentally. There are even metal pairs (e.g., Pd and Ni) where even if the fraction of radicals reaching each catalyst were extremely different, the performance would not

be similar. To be sure, the collision of N and H radicals with surface-bound species to make ER reactions is unlikely to be 100% effective. But **Fig. 4c**, which plots TOFs for different efficacies of ER reactions (as given by different S_{0ER}values), shows that in a scenario where all N and H radicals in the bulk phase (ρ = 1.0), collisions of N and H radicals with surface-bound species only need to be around 10^{-8} % effective to get all metals to present TOF_{NH3} values within similar orders of magnitude. Albeit to generate the same kind of performance similarity, the efficacy of collisions would need to be correspondingly higher if the fraction of radicals reaching the catalyst is correspondingly lower.

Although N and H radicals can act as an "equalizer" factor across metals, we can use all plots in **Fig. 4** to briefly discuss the different *main* mechanistic impacts of N and H radicals on each metal. For the nitrophobic metals (as measured by N binding energy[3]), Au and Ag, the threshold fraction ρ of N and H radicals needed to boost TOF_{NH3} is as small as 10^{-37}. For the remaining (non-nitrophobic metals), the threshold fraction ρ is higher, ranging from ~10^{-20} (for Fe) to ~10^{-15} (for Pd), increasing with *nitrophobicity*. This apparent contradiction in trends with nitrophobicity occurs because the initial boosting mechanism is different between the two groups of metals. In Au and Ag, the initial boost occurs primarily because of N radicals providing a source for N* via *r11*, whereas in the non-nitrophobic metals (Pd, Cu, Ni, Co, Fe) the initial boost primarily occurs because of H radicals opening up new hydrogenation pathways, e.g., via ER reactions *r14 and r15*. A higher fraction of H radicals reaching the surface is

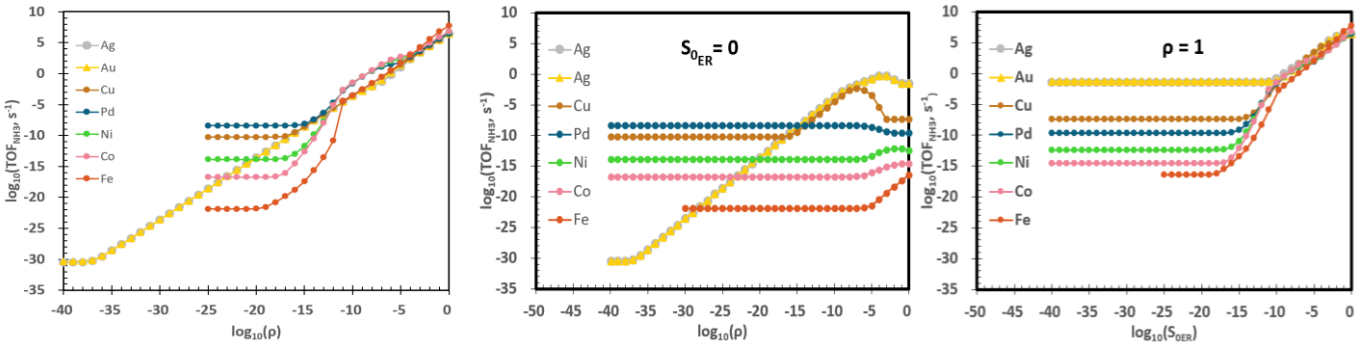

Fig.4. TOFs for NH_3 on studied metals for different fractions (ρ) of radicals reaching the catalyst surface and different efficacies (S_{0ER}) of ER reactions. a) Variable ρ and S_{0ER} equal to one. b) Variable ρ and S_{0ER} equal to zero. c) Variable S_{0ER} and ρ equal to one. Specifically, ρ is the ratio between partial pressure of N and H radicals immediately above the catalyst surface and the partial pressure of these radicals in the bulk (1.9 x 10-4 bar for N and 1.5 x 10^{-2} bar for H), and S_{0ER} is the sticking coefficient.

needed for ER hydrogenation to compete with LH hydrogenation as nitrophobicity increases, because LH hydrogenation pathways (*r7-r9*) are generally easier the more nitrophobic the metal is. [3]

The point that ER hydrogenation more easily competes with LH hydrogenation as metal *nitrophilicity* increases is readily made by **Fig. 4c**. This figure reveals that the threshold sticking coefficient S_{0ER} to boost TOF_{NH3} at fixed ρ increases from Fe to Au. Interestingly, the close competition between ER and LH hydrogenation at *some* fractions of radicals reaching the surface is manifested in the s-shape relationship between TOF_{NH3} and ρ for non-nitrophobic metals in **Fig. 4a**. At the beginning of the non-linear part of these s-shaped relationships, ER hydrogenation start to contribute to NH_3 formation, but LH hydrogenation is dominant. The end of the non-linear part of the relationships is dictated by the complete takeover of ER over LH hydrogenation. Importantly, even for the nitrophobic Au and Ag, eventually, additional boost in TOF_{NH3} as ρ continues to increase is due to ER hydrogenations.

Albeit not apparent from the linear shape of the relationship between TOF_{NH3} and ρ for Au and Ag in **Fig. 4a**, the boosts in TOF_{NH3} beyond ρ ~10^{-10} primarily originate from radicals enabling ER reactions (as evidenced from changes in the dominant route connecting N* to NH_3*, *vide infra*). This is perhaps apparent with the boost in TOF_{NH3} observed for Au and Ag once S_{0ER} reaches ~10^{-10} in **Fig. 4c** (note that the rate of ER reactions is proportional to the product of ρ and S_{0ER}, so mathematically their effect on how easily ER reactions occur is equivalent). Finally, without ER reactions, there is a limit to the benefits of N and H radical adsorption providing N* and H*, as beyond some ρ values TOF_{NH3} no longer increases (or even decreases, in the cases with higher nitrophobicity). Beyond that point, metal ordering based on TOF_{NH3}, and *orders of magnitude differences* between TOF_{NH3} values, would be consistent with NH_3 formation being primarily controlled by LH hydrogenation.

On the extent N radicals contribute to N_2H_Y* formation. Earlier work by us found that enthalpic barriers for ER reactions of surface-bound species with N and H radicals are negligible.[3] This finding suggested that these ER reactions could plausibly generate the N_2H_Y detected in some plasma-catalysis experiments.[3,13,15,17] Surface-bound N_2H_Y* may open up the associative mechanism often discussed for electrocatalytic NH_3 formation,[36–38] where N_2H_Y gets hydrogenated until eventually the species splits into NH_n and NH_m (where $n + m = y$). In this

subsection we leverage our microkinetic model to examine whether such N_2H_Y detection can only be explained through ER reactions involving N and H (*r17-r30*). To establish a baseline, first we examined the concentration of N_2H_Y species in the thermocatalytic model, which in our case also contains reactions for the associative mechanism (*r31-r52*) usually ignored in the literature when discussing the HB process—the associative mechanism starts with the hydrogenation of N_2*.

At the tested conditions (400 K and 1 bar), we found the relative contribution of the associative mechanism to TOF_{NH3} to be sizable. Indeed, neglecting to include the reactions relevant to the associative mechanism in our model decreased the calculated TOF_{NH3} by orders of magnitude (except for Fe) and changed relative metal performances (**Fig. S2**). Still, in absolute terms, the calculated TOF_{NH3} values across metals were extremely low and the total *fractional* coverage of N_2H_Y species ($\theta_{N_2H_Y}$) ranged from ~10^{-36} to ~10^{-17}, with the highest values being from the metals with moderate nitrophilicity (Co and Ni) (**Fig. S3**). Before proceeding to compare these coverages with the case where ER reactions involving plasma radicals occur, we considered that in the latter case the extent of N_2H_Y formation would presumably depends on how easily ER reactions occurs. Thus, we decided to go beyond our baseline case and test several scenarios varying: *i)* the fraction of N and H radicals that reach the catalyst surface ρ, *ii)* the sticking coefficient for ER reactions S_{0ER}, and *iii)* the entropy loss assumption for the transition state of ER reactions.

To choose which scenarios to focus on, we first ran the microkinetic model sweeping both ρ and S_{0ER} from 1 x 10^{-15} to 1 for both our entropy loss assumption ($\Delta S^{\neq}$ = 1/3 $S_{l\text{-gas}}$) and that of Engelmann *et al.* ($\Delta S^{\neq}$ = $S_{l\text{-gas}}$). Then, for each

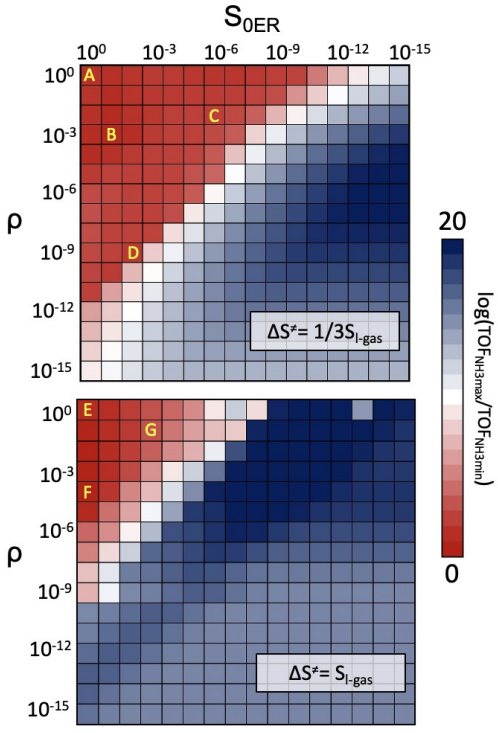

Fig. 5. Differences in orders of magnitude between highest (TOF_{NH3max}) and lowest ((TOF_{NH3min}) NH_3 turnover frequency across metals for different combination of ρ, S_{0ER} and $\Delta S^{\neq}$ in the microkinetic model. Baseline reaction conditions for the model are identical to those in Fig, 2.

combination of ρ, S_{0ER} and $\Delta S^{\neq}$ assumption, we collected the difference in orders of magnitude between the highest and lowest TOF_{NH3} across metals. As shown in **Fig. 5**, there are multiple combinations of ρ, S_{0ER} and $\Delta S^{\neq}$ assumption that produces values of TOF_{NH3} relatively close in order of magnitude across metals—consistent with similarity in reaction rates observed in experiments, and thus having a higher probability of being the "correct" assumption. We chose a diverse set of scenarios (points A through G noted in **Fig. 5**) to examine N_2H_Y formation.

Fig. 6 shows that the total fractional coverage $\theta_{N_2H_Y}$ ranges from ~10^{-12} to ~10^{-1} across the seven chosen scenarios. This range of N_2H_Y fractional coverage is orders of magnitude higher than the ~10^{-36} to ~10^{-17} range for the baseline "thermal" case. Furthermore, examination metal by metal indicates that, in scenarios where ER reactions involving N and H radicals occur, N_2H_Y coverages are expected to increase by *at least* thirteen orders of magnitude relative to scenarios when said ER reactions do not occur. Accordingly, without N and H radicals reaching the catalyst surface and opening new reaction pathways, the reported experimental detection of surface-bound N_2H_Y species via techniques such as FTIR seems dramatically less likely.

4.2. Mechanistic insights as a function of radical abundance, ease of ER reactions, and catalyst nitrophilicity.

On the dominant pathways leading to NH_3 formation. To identify the most dominant pathways leading to NH_3*, in

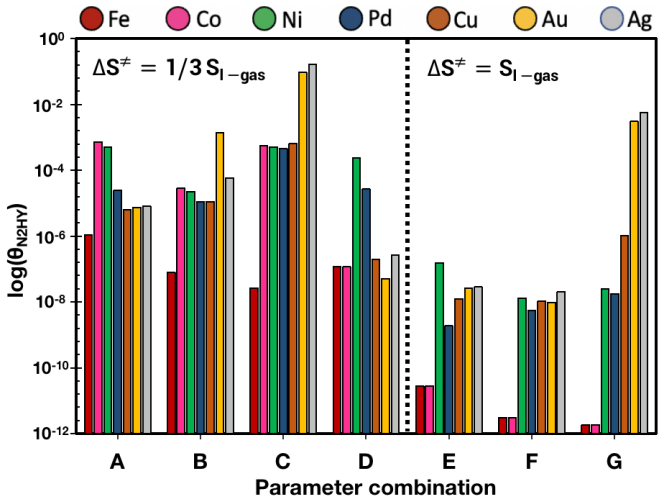

Fig. 6. Total fractional coverage of N_2H_Y species calculated under different parameter scenarios in the microkinetic model. Scenarios A through G correspond to specific values of ρ, S_{0ER} and $\Delta S^{\neq}$ pointed in

Fig. 5. Baseline reaction conditions for the model are identical to those in Fig, 2.

scenarios that yield a narrow distribution of TOF_{NH3} across metals akin to experimental rate trends we inspected the reaction rates within the reaction networks emerging from scenarios A through G. We found that the sequence NH* ⟶ NH_2* ⟶ NH_3* was a dominant feature across all scenarios, despite the presence of N_2H_Y forming pathways. In other words, most NH_3* comes from NH_2* hydrogenation, which in turn mostly comes from NH* hydrogenation, with decomposition of N_2H_Y species being a minority contributor to NH_3* and NH_2* formation. Another common feature across scenarios and metals is that not all formed NH_2* is converted into NH_3*, but a minority of it is converted to N_2H_2* through ER reaction with N radicals (*r18*). The above observations are visually conveyed in the reaction flux diagrams for scenarios A and D for Fe, Ni and Au in **Fig. 7**—scenarios E and F are shown in **Fig. S5**. However, we now proceed to discuss subtle differences related to the dominant pathway that can be observed depending on the nitrophilicity of the catalyst, the abundance of radicals in the plasma environment that the catalyst sees (which depends on ρ) and the inherent ease of ER reaction (which depends on by S_{0ER} and $\Delta S^{\neq}$).

Although across all inspected scenarios, a major source of NH* was the hydrogenation of N*, in scenarios such as E for Ni, nitrogenation of H* through an ER mechanism (*r16*) was *somewhat* more prominent (**Fig. S5**). Similar to hydrogenation of NH_X and N_2H_Y in general, the hydrogenation of N* to produce NH* tended to be dominated by the ER mechanism. But some instances of dominance by the LH mechanism were observed for this hydrogenation step (and other hydrogenation steps), more commonly in scenarios combining poor radical availability and high metal nitrophobicity. For instance, consider the (nitrophobic) Au case

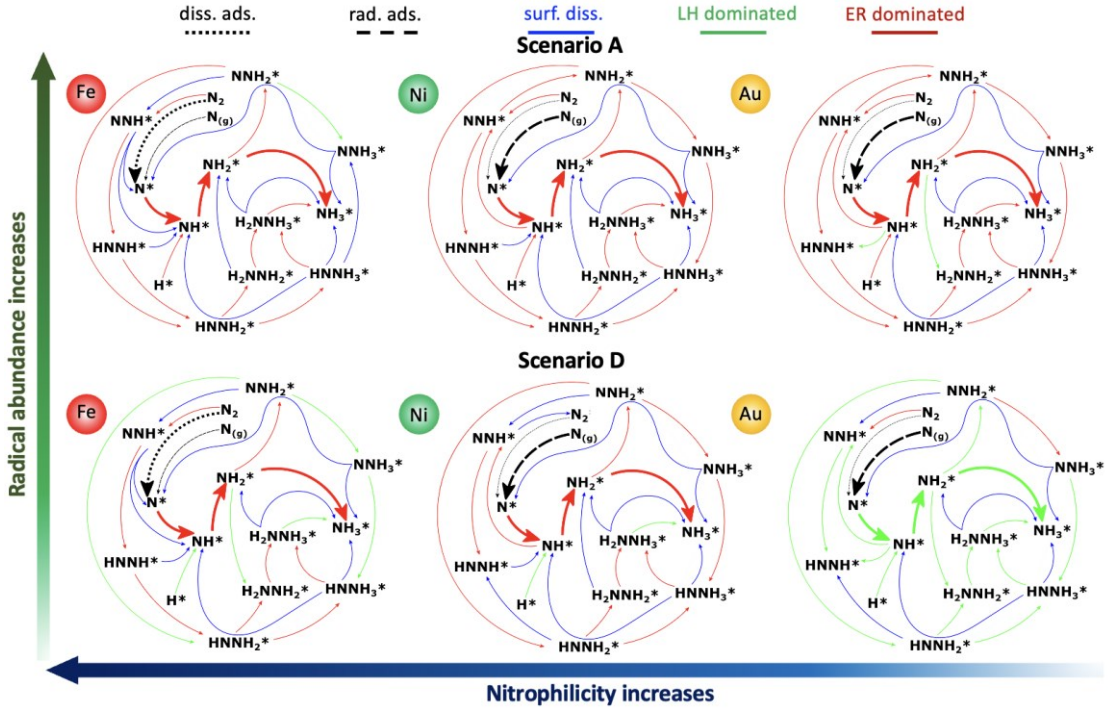

Fig. 7. Reaction flux diagrams for Fe, Ni, and Au obtained for scenarios A and D, which correspond to specific values of ρ, S_{0ER} and $\Delta S^{\neq}$ pointed in Fig. 5. For simplicity, diagrams are primarily centered around N_XH_Y species. As there is usually more than one possible reaction connecting two species, the connection is drawn based on the most important reaction connecting the species. The species N_2 in the diagram refer to either N_2* or $N_{2(g)}/N_2(v)$ as inferred from context given by the relevant arrow. Color, thickness, and direction of the connection indicates the type, rate, and dominant direction of the most important reaction connecting the species. Baseline reaction conditions for the model are identical to those in Fig. 2.

shown in scenario D ($\rho \sim 10^{-9}$) in **Fig. 7**. Remarkably, and testament to the inherent facility of LH hydrogenation in nitrophobic metals, is that these metals can in some scenarios yield similar TOF_{NH3} values as nitrophilic metals without having to rely on ER hydrogenation through all the steps in the dominant NH_3 formation pathway (e.g., consider Au in scenarios D, E, and F).

An additional difference stemming from differences in metal nitrophilicity is the source for N* across the studied scenarios. In (the highly nitrophilic) Fe, the primary source of N* was persistently the dissociative adsorption of N_2 gas species ($N_{2(g)}$ and $N_2(v)$), while for all other metals was the adsorption of plasma N radicals (*r11*). Note that earlier was noted that, as ρ increased, Ni (a mid nitrophilicity metal) would first get a TOF_{NH3} boost from ER hydrogenation instead of N radical adsorption. However, the ρ values associated with

scenarios A through G are high enough to let N radical adsorption also takeover as the primary source of N*. Another subtle difference tied to nitrophilicity differences is that the more nitrophilic the metal is, the earlier N_2H_Y species tend to decompose into NH_X species. While this is more difficult to appreciate solely by looking at the diagrams, consider that in Fe N_2H* tends to dissociate to yield NH* across all scenarios. On the other hand, in Au the reverse is preferred, with NH* nitrogenation to form N_2H* outpacing N_2H* dissociation.

On the kinetic relevance of N_2H_Y-forming pathways. The experimental detection of N_2H_Y species does not necessarily mean that these species are kinetically relevant (i.e., N_2H_Y could be a spectator species). On the other hand, the complexity and multitude of N_2H_Y-forming pathways in diagrams such as those in **Fig. 7** makes it unclear to conclude if overall the presence of N_2H_Y-forming routes has an impact on calculated TOF_{NH3} values. Thus, here we do a simple exercise where we turn "on" and "off" the N_2H_Y-forming routes in our model an examine differences on calculated TOF_{NH3} values. For instance, in the thermal case (**Fig. S3**), while TOF_{NH3} values were consistently negligible across metals, the addition of N_2H_Y-forming routes via the associative mechanism notably increased TOF_{NH3} in metals other than Fe. Thus, to discuss the kinetic relevance of N_2H_Y species in the plasma case, we calculate the parameter λ:

$$\lambda = \frac{TOF_{NH3_{N2HY-ON}}}{TOF_{NH3_{N2HY-OFF}}} - 1 \qquad (8)$$

for the scenarios A through G that we have discussed so far.

To convey the change in order of magnitude for TOF_{NH3} when N_2H_Y pathways are "on," **Fig. 8** shows a heat map based on $\log|\lambda|$. Some trends can be observed, despite being apparent that the calculated kinetic impact of N_2H_Y-forming pathways largely depends on model assumptions—

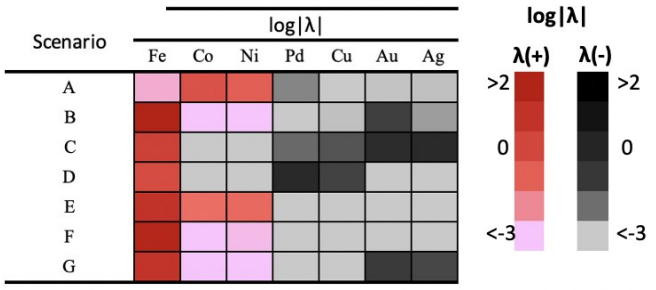

Fig. 8. Impact of N_2H_Y-forming reactions on TOF_{NH3} in different scenarios. Color conveys the order of magnitude of the impact as given by $\log|\lambda|$. Red scale is used to indicate a positive impact and black scale is used for negative impact. Baseline reaction conditions for the model are identical to those in Fig. 2.

e.g., the fraction of N and H radicals reaching the catalyst surface (ρ), as well as S_{0ER} and $\Delta S^{\neq}$—that modulate the rate at which ER reactions occur. One trend is the tendency for N_2H_Y-forming pathways to have a negative impact on nitrophobic metals (e.g., Au), and a positive impact on nitrophilic metals (e.g., Fe). However, instances of negative impact tended to be less dramatic than instances of positive impact. For instance, in six of the seven tested scenarios, the calculated TOF_{NH3} for (nitrophilic) Fe underwent an increase between ~70% and ~15000% when N_2H_Y forming pathways were included in the microkinetic model. On the other hand, for (nitrophobic) Au, the inclusion of these pathways led to a decrease in TOF_{NH3} between 4% and 40% in three of the seven tested scenarios.

While there are several factors in play, the above trends can be largely understood considering that formation of N_2H_Y species has the potential to provide a parallel route to yield NH_3* (**Fig. 7**), contingent on their eventual splitting into NH_n and NH_m ($n + m = y$). As dissociation (desorption) barriers of N_2H_Y species are lower (higher) in nitrophilic than in nitrophobic metals, the former metals are better poised to benefit from the parallel route—notice that N_2H_Y desorption outcompeting its dissociation reduces nitrogen availability for ammonia formation. But regardless of whether the impact of N_2H_Y-forming pathways is positive or negative, the extent of the impact could potentially make a difference if one aspires to develop sufficiently predictive models as to correctly capture relative catalyst performance for plasma-assisted NH_3 synthesis (where metal performances tend to be closer than in thermal catalysis).

On the kinetic relevance of N and H dissolution reactions. Partly motivated by the idea that the catalyst surface could get "oversaturated" due to the adsorption of atomic plasma radicals, some works in plasma catalysis have discussed the potential impact of dissolution of atomic species into the catalyst subsurface.[39–42] Along these lines, for plasma-catalytic NH_3 synthesis, others[43,44] and us [18] have brought up the possibility of a "hydrogen sink" effect, where the catalyst subsurface may act as a reservoir of atomic hydrogen for subsequent hydrogenation

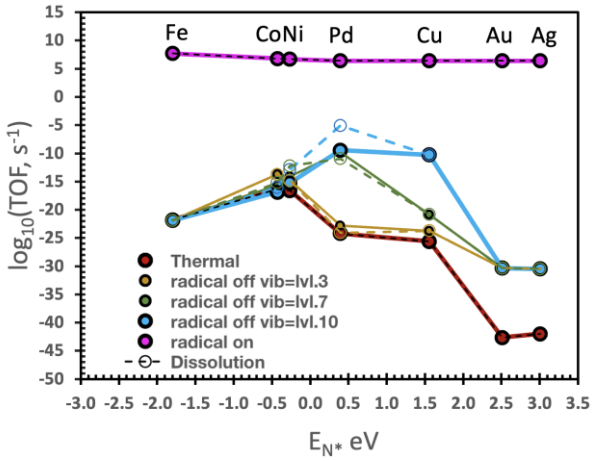

Fig. 9. Comparison of TOF_{NH3} values when dissolution reactions are included (solid lines) and excluded (dash lines) for SSSR = 10. Case scenarios include *i)* only standard reactions for thermal catalysis (red), *ii)* dissociation reactions for $N_2(v)$ added to the "red" model, considering excitations until v = 3 (yellow), v = 7 (green) or v =10 (blue), and *iii)* N and H radical adsorption and ER reactions added to

the "blue" model (purple). Baseline reaction conditions are identical to those in Fig, 2.

reactions, while also inhibiting the loss of catalyst-bound, atomic hydrogen via ER "recombination" reactions (*r54*). Thus, to examine *i)* whether dissolutions effects—quantified by changes in TOF_{NH3} when dissolution reactions occur—are significant in plasma-assisted NH_3 synthesis—and/or *ii*) the conditions necessary for dissolutions effects to be significant—we added the dissolution reactions below:

$$N^* + \Diamond \longrightarrow N\Diamond + * \qquad (r55)$$

$$H^* + \Diamond \longrightarrow H\Diamond + * \qquad (r56)$$

which consider the dissolution of atomic hydrogen and nitrogen to subsurface sites (as has been shown to occur in metallic membranes [45,46]), and where ◊ indicates a free subsurface site.

For the case where the subsurface to surface sites ratio (SSSR) is equal to one, an equation analogous to Eq. 1 is added to the model:

$$\frac{\partial \emptyset_i}{\partial t} = \sum_j^m c_{i,j}\ r_j \qquad (9)$$

where $\emptyset_i$ is the fractional occupation of subsurface sites by species i (here atomic H or N). The reaction rate r_j is still calculated with Eq. 2, albeit considering that $a_{f,j}$ and $a_{b,j}$ can also correspond to $\emptyset_i$ values. Analogous to Eq. 3, the subsurface site balance is added to the model:

$$1 = \sum_i^n \emptyset_i + \emptyset_\Diamond \qquad (10)$$

For SSSR equal to one, changes in TOF_{NH3} were negligible in all studied scenarios, indicating such "reservoir size" to be too small to engender dissolution effects. Thus, to consider larger reservoir sizes (albeit to a first approximation), during the integration procedure, the rate calculations at time $t + \Delta t$ used the values of $\emptyset_i$ obtained at t but divided by SSSR. However, only until the reservoir featured at least ten times as many sites as surface sites (SSSR = 10), we started to see some impact of dissolution reactions on TOF_{NH3}, and only under "radical-poor" plasma scenarios, and only for Pd (**Fig. 9**). For instance, dissolution effects were observed on Pd when only vibrationally excited plasma species (but no plasma radicals) are assumed to reach its surface. For instance, when vibrationally excited $N_2(v)$, with v up to ten, a TOF-increasing dissolution effect was observed, seemingly stemming from a favorable change in the "balance" between N* and H* coverages. Namely, in this particular case, dissolution reactions drove the surface away from near saturation with N* (θ_{N*} from ~98% to ~45%) and away from near H* absence (θ_{H*} from ~0.03 % to ~4%), creating a friendlier surface environment for LH hydrogenation, which is the dominant type of hydrogenation that leads to NH_3* in the absence of radicals.

Accordingly, when dissolution effects occur, they seem to generally originate from dissolution-driven changes in the balance between N* and H* coverages that more directly affect LH reactions. This partly explains why dissolution effects tend to go away when the catalyst is assumed to "see" a radical-rich environment (**Fig. 9**, for which ρ= 1.0). Namely N and H radicals activate ER reactions that in turn activate pathways to NH_3* formation that are less sensitive to changes in surface coverage. But if the plasma environment "seen" by the catalyst is assumed to be sufficiently radical-poor—e.g., $\rho \sim 1.0 \times 10^{-9}$ to 1.0×10^{-8} depending on the entropy loss assumption)—dissolution start to emerge again, with the magnitude of the effect becoming more pronounced as the reservoir is made to increase in size (**Fig. S6**). However, whether the emerging dissolution effects were beneficial or not was sensitive to the assumed entropy loss for ER reactions (**Fig. S6**).

But relatively robust to model assumptions, the exercise done in this subsection allows us to affirm that dissolution reactions seem to be kinetically relevant *only* when all the following conditions are met: *i)* the plasma environment the catalyst "sees" is radical-poor, *ii)* the catalyst operates at high coverage, *iii*) dissolution energy barriers are low, and *iv)* "reverse" dissolution barriers are at least moderate. If conditions *i* through *iv* are met, then the strength of dissolution effects does depend on the size of the "reservoir." Among the studied metals, however, only Pd seemed amenable to meet conditions "*ii*" (due to moderate nitrophilicity) and "*iii/iv*" (E_a values are 51 kJ/mol and 26 kJ/mol for dissolution reactions *r55* and *r56*, respectively). Hence, that we did not observe dissolution effects in metals such as Ag and Au (regardless of reservoir size, **Fig. S7**) is primarily explained by their high nitrophobicity, which have them operate at low N* and H* coverages (θ_{N*} and θ_{H*} less than 5%). That we did not observe dissolution effects in metals such as Fe is primarily explained by large dissolution barriers (E_a are 190 kJ/mol and 97 kJ/mol for *r55* and *r56*, respectively)—note, however, that here we did not consider dissolution barrier reduction effects that some

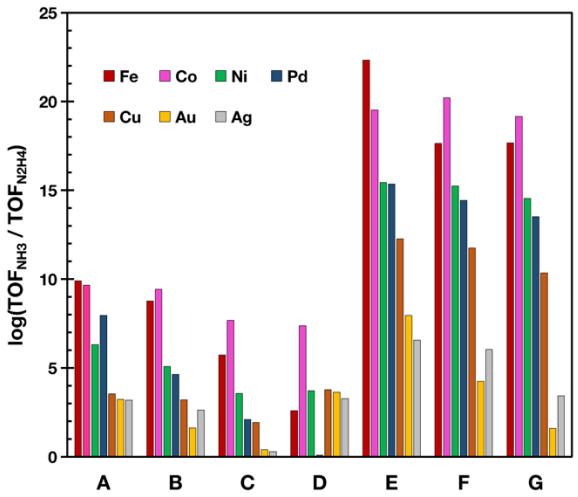

Fig. 10. Differences in order of magnitude for ammonia and hydrazine production under different scenarios for plasma-catalyst interactions/reactions (A through G indicated in Fig. 5). Differences are captured by the logarithm of the ratio of TOF_{NH3} and TOF_{N2H4}. Baseline reaction conditions are identical to those in Fig, 2.

authors [39] have predicted may occur under the high coverages nitrophilic metals tend to operate under plasmas (*vide infra*).

Competing N_2H_Y products. Some earlier works reported the formation of hydrazine (N_2H_4) during plasma-assisted NH_3 synthesis.[47,48] As formation of N_2H_Y products is possible in our calculations (tied to the inclusion of N_2H_Y-forming pathways in our microkinetic model), we examined to what extent these side products would form under different scenarios. For instance, **Fig. 10** presents the ratio between the orders of magnitude of NH_3 and N_2H_4 production rates (as given by logarithm of TOF_{NH3}/TOF_{N2H4}) for the scenarios A through G discussed in detail in this work. Generally, the more nitrophilic the metal is, the less significant the production of N_2H_4 is. For instance, in Fe, TOF_{NH3} is always at least three orders of magnitude higher than TOF_{N2H4}. This is consistent with barriers for nitrogen bond dissociation in N_2H_Y species decreasing with nitrophilicity,[3] which also partly explain N_2H_Y-forming pathways tending to have a positive effect on TOF_{NH3} in nitrophilic metals (**Fig. 8**). Namely, instead of forming competing N_2H_Y products, N_2H_Y intermediates readily decompose into NH_X species that eventually hydrogenate to NH_3.

On the other hand, N_2H_4 production (relative to NH_3 production) tends to be more significant in nitrophobic metals such as Au (relative to nitrophilic metals). This is consistent with barriers for nitrogen bond dissociation in N_2H_Y species decreasing with nitrophilicity.[3] Thus, the higher nitrogen bond dissociation barrier in nitrophobic metals allows N_2H_4 a better chance to desorb before breaking into NH_X species. This also partly explains why N_2H_Y-forming pathways tend to (barely) negatively affect TOF_{NH3}. Although N_2 hydrogenation offers an alternative route to (eventually) split the nitrogen bond, this is essentially counterbalanced by N_2H_Y desorption. Still, in nitrophobic metals we still find N_2H_4 production to be very low

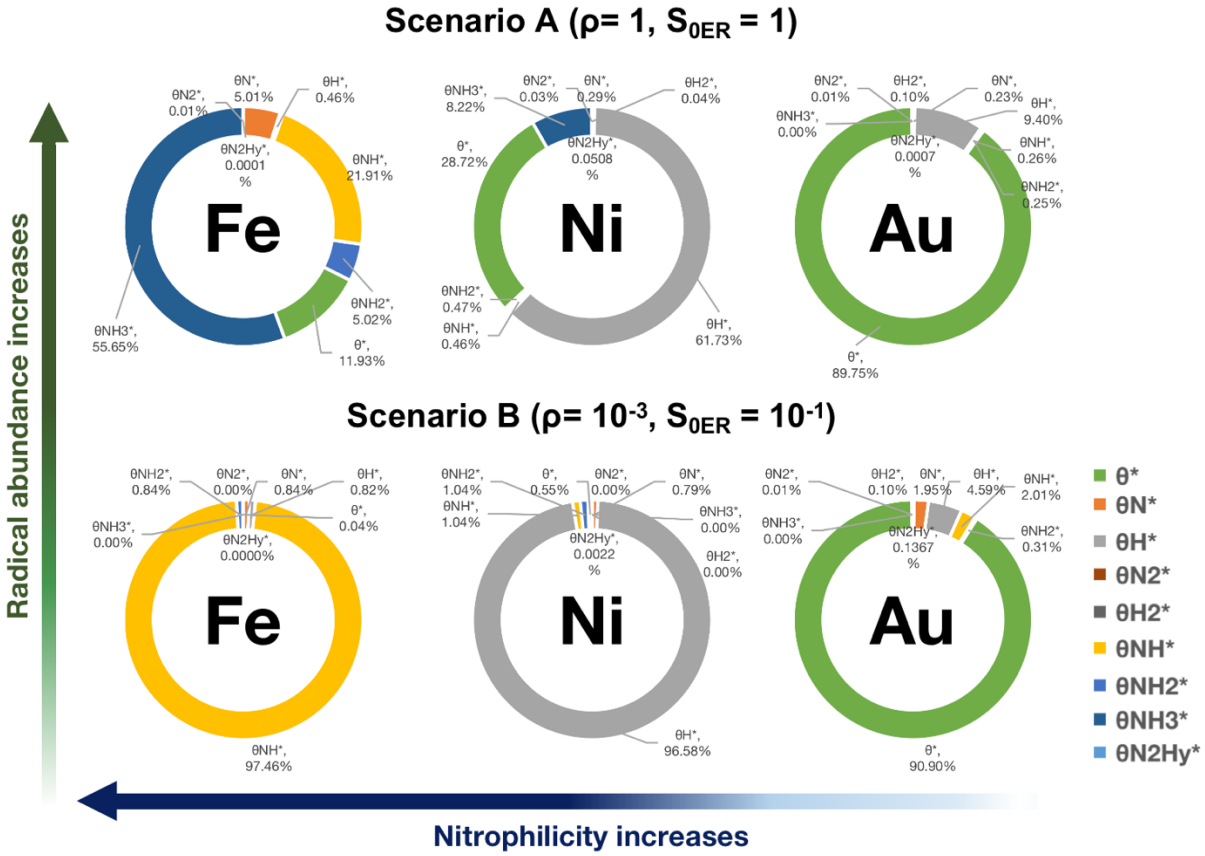

Fig. 11. Example of differences in catalyst adlayer composition (i.e., fractional coverages) predicted by microkinetic modeling under different plasma/reaction scenarios (here scenario A and B).

relative to NH_3 production with the exception of a few metal-scenario combinations. Similar observations are made for N_2H_2 production, whose rate comparisons are shown in **Fig. S8**.

Potential strategies to zero-in onto correct model assumptions. At this point note that a recurring theme in the discussion in this work is that different scenarios (i.e., different model assumptions) lead to some differences in predictions about rate trends, product distributions, among others, some of which are amenable to experimental verification, potentially allowing to discard incorrect assumptions or confirm correct ones. An example of this was our own exercises in earlier sections showing that trends in experimental rates across metal—or the increase in ammonia formation rates for Fe relative to the thermal case—were probably only possible if N

and H radicals reach the catalyst surface. From the previous subsection, one could infer that setting up experiments to measure N_2H_4 production (or lack thereof) may serve as a way to discard/verify model assumptions. For instance, it seems that a scenario where one hundredth of bulk plasma N and H radicals reach the catalyst surface *and* ER reactions have sticking coefficients in the order of a millionth (scenario C) seem unlikely as this would imply that comparable formation of NH_3 and N_2H_4 should be experimentally observed.

While the above are some general conclusions that shed light into plasma-catalytic NH_3 synthesis, to push the understanding of plasma catalysis to the point where it can be predictive and leveraged for rational design, it is still necessary to understand exactly how (and to what extent) plasma species interact with the catalyst. Indeed, several experimental studies have looked for clever ways to characterize the catalyst to understand the interaction of plasma species with it.[9,10,19,20,49] In this final subsection, we propose the sensitivity of the composition of the adsorbed layer (adlayer) of the catalyst to different "interaction scenarios" as potentially leverageable to design future characterization experiments that could clarify the correct scenario (e.g., the plasma composition that the catalyst "sees") that should be introduced into microkinetic models.

To illustrate the idea above consider the adlayer compositions (fractional coverages) presented for Fe, Ni and Au for scenarios A and B in **Fig. 11** (all other scenarios are presented in **Fig. S9**). Notice that in a scenario where all plasma bulk N and H radicals reach the catalyst surface and react efficiently (scenario A), Fe would be primarily covered by NH_3* (θ_{NH_3*}~0.56). However, if only a thousandth of bulk radicals reach the surface (ρ= 10^{-3}) and react somewhat less efficiently ($S_{0ER} = 10^{-1}$), as in scenario B, Fe would be primarily covered with NH* (θ_{NH*}~0.98). To be sure, there can be metals whose adlayer composition is not dramatically different between two scenarios. For instance, in both A and B scenarios, Au appears to have its surface mostly empty (θ_* ~0.90) with some low H* coverage (θ_{H*} ~0.95 and θ_{H*} ~0.50, respectively). Accordingly, to reduce ambiguity, it would be recommendable to set up characterization experiments with several metals and consider their adlayer compositional "signatures" together. In other words, one would aim to identify an interaction (reaction) scenario between radicals and catalyst that is simultaneously consistent with adlayer compositions across different metals. Also notice that while plots in **Fig. 11** focus on the "major" components of the adlayer (i.e., NH_Y species), accurate characterization of the "minor components (i.e., N_2H_Y species) could provide an additional way for disambiguation.

CONCLUSIONS

DFT-informed microkinetic models (using the mean-field approximation) where the catalyst was assumed to "see" a "minimal" plasma of a given composition were used to computationally study the formation of NH_3 under plasma environments. Some distinctions with earlier efforts in the literature include, but are not limited to, the addition of N_2H_Y-forming routes and dissolution reactions in the models. Specifically, through sensitivity analysis to *i)* the inclusion/exclusion of plasma species and/or reactions in the model, and *ii)* assumptions for the concentration of plasma species present in the minimal plasma, and *iii)* assumptions for reaction parameters, we sought to computationally decouple the effects of select plasma species, reactions, and reaction parameters on NH_3 (and N_2H_4) turnover frequencies, dominant reaction pathways, and catalyst adlayers compositions.

Contrasting trends predicted from modeling against key experimental observations (including rate trends obtained here for Fe, Ni and Ag in a DBD reactor at different input powers) seems to support the thesis that N and H radicals are kinetics-controlling species for the plasma-catalytic formation of NH_3. In modeling scenarios where predicted ammonia TOFs across metals are relatively close to each other (as experimentally observed) we find that *i)* N radicals seem to primarily act as a source of N* (more prominently in nitrophobic metals such as Au/Ag), while H radicals seem to primarily facilitate hydrogenation through ER reactions (more prominently in nitrophilic metals) *ii)* NH_3 formation seemed to be consistently dominated by the NH* ⟶ NH_2* ⟶ NH_3* reaction sequence, yet we found scenarios in which N_2H_Y-forming pathways could boost (dampen) ammonia production in nitrophilic (nitrophobic) metals, *iii)* dissolution effects seem to be only plausible in "radical-poor" environments, provided that the catalyst operates at high coverage and features low dissolution barrier for N and H (here only Pd met those conditions), *iv)* despite the inclusion of N_2H_Y-forming pathways, predicted formation of side products such as N2H4 hydrazine was negligible in most scenarios.

As several potentially useful predictions were sensitive to model assumptions, we propose that some of these assumptions could be potentially clarified through *in situ* compositional analysis of catalyst adlayers (e.g., the fraction of radicals from the plasma bulk that reach the catalyst surface), as the adlayer composition seems to be rather sensitive to the plasma environment assumed to be "seen" by the catalyst. Additionally, as some of the assumption pertain to values of sticking coefficients, independent studies aiming to accurately estimate these coefficients could further help reduce the uncertainty of model predictions (and insights therein).

Aspects that were not considered in this work are coverage effects, which may have some impact, especially on activation energies of LH reactions of the most nitrophilic metals, as these metals tend to work at higher coverages. Charged species may also play a role but were not considered here, because they are expected to be less abundant than radicals, and the addition of radicals already seem to explain experimental rate trends. Finally, note that the kinetic relevance of plasma radicals evinced in the work herein for NH_3 synthesis

suggests that plasma radicals may also play a key role in other plasma-catalytic processes.

SUPPORTING INFORMATION

Reactor setup and details on rate calculations, experimental optical emission spectroscopy and rate data, TOFs and N_2H_Y coverage for thermocatalytic ammonia synthesis, reaction flux diagrams for scenarios E and F, TOFs as function of subsurface reservoir size, comparison of TOFs for NH_3 and N_2H_2, predicted adlayer compositions for scenarios A through G.

ACKNOWLEDGEMENTS

D.A.G.-G. and M.L.C acknowledge funding from the National Science Foundation through collaborative grants CBET-1921484 and CBET-2203166. Simulations were made possible by the Mio supercomputer cluster at Colorado School of Mines and NERSC computational resources from the U.S. Department of Energy (DOE).

REFERENCES

(1) Ghavam, S.; Vahdati, M.; Wilson, I. A. G.; Styring, P. Sustainable ammonia production processes. *Front. Energy Res.* **2021**, *9*.

(2) Li, C.; Wang, T.; Gong, J. Alternative strategies toward sustainable ammonia synthesis. *Trans. Tianjin Univ.* **2020**, *26*, 67–91.

(3) Liu, T.-W.; Gorky, F.; Carreon, M. L.; Gómez-Gualdrón, D. A. Energetics of Reaction Pathways Enabled by N and H Radicals during Catalytic, Plasma-Assisted NH_3 Synthesis. *ACS Sustain. Chem. Eng.* **2022**.

(4) Natural Gas Weekly Update U.S. Energy Information Administration - EIA - Independent Statistics and Analysis https://www.eia.gov/naturalgas/weekly/archivenew_ngwu/2021/04_01/ (accessed Apr 20, 2023).

(5) Fu, R.; Feldman, D.; Margolis, R.; Woodhouse, M.; Ardani, K. *U.S. solar photovoltaic system cost benchmark: Q1 2017*; EERE Publication and Product Library, 2017.

(6) Zeng, Z.; Ziegler, A. D.; Searchinger, T.; Yang, L.; Chen, A.; Ju, K.; Piao, S.; Li, L. Z. X.; Ciais, P.; Chen, D.; et al. A reversal in global terrestrial stilling and its implications for wind energy production. *Nat. Clim. Chang.* **2019**, *9*, 979–985.

(7) Carreon, M. L. Plasma catalysis: a brief tutorial. *Plasma Res. Express* **2019**, *1*, 043001.

(8) Kim, H.-H.; Teramoto, Y.; Ogata, A.; Takagi, H.; Nanba, T. Atmospheric-pressure nonthermal plasma synthesis of ammonia over ruthenium catalysts. *Plasma Process. Polym.* **2017**, *14*, 1600157.

(9) Rouwenhorst, K. H. R.; Burbach, H. G. B.; Vogel, D. W.; Núñez Paulí, J.; Geerdink, B.; Lefferts, L. Plasma-catalytic ammonia synthesis beyond thermal equilibrium on Ru-based catalysts in non-thermal plasma. *Catal. Sci. Technol.* **2021**, *11*, 2834–2843.

(10) Barboun, P. M.; Mehta, P.; Herrera, F.; Go, D. B.; Schneider, W. F.; Hicks, J. C. Distinguishing Plasma Contributions to Catalyst Performance in Plasma-Assisted Ammonia Synthesis. *ACS Sustain. Chem. Eng.* **2019**, *7*, 8621–8630.

(11) Rouwenhorst, K. H. R.; Kim, H.-H.; Lefferts, L. Vibrationally Excited Activation of N_2 in Plasma-Enhanced Catalytic Ammonia Synthesis: A Kinetic Analysis. *ACS Sustain. Chem. Eng.* **2019**, *7*, 17515–17522.

(12) Mehta, P.; Barboun, P. M.; Engelmann, Y.; Go, D. B.; Bogaerts, A.; Schneider, W. F.; Hicks, J. C. Plasma-Catalytic Ammonia Synthesis beyond the Equilibrium Limit. *ACS Catal.* **2020**, *10*, 6726–6734.

(13) Zhao, H.; Song, G.; Chen, Z.; Yang, X.; Yan, C.; Abe, S.; Ju, Y.; Sundaresan, S.; Koel, B. E. *In Situ* Identification of NNH and N_2 H_2 by Using Molecular-Beam Mass Spectrometry in Plasma-Assisted Catalysis for NH_3 Synthesis. *ACS Energy Lett.* **2021**, 53–58.

(14) Mehta, P.; Barboun, P.; Herrera, F. A.; Kim, J.; Rumbach, P.; Go, D. B.; Hicks, J. C.; Schneider, W. F. Overcoming ammonia synthesis scaling relations with plasma-enabled catalysis. *Nat. Catal. 1.4 (2018): 269-275*.

(15) Winter, L. R.; Ashford, B.; Hong, J.; Murphy, A. B.; Chen, J. G. Identifying surface reaction intermediates in plasma catalytic ammonia synthesis. *ACS Catal.* **2020**, *10*, 14763–14774.

(16) Shah, J.; Wang, W.; Bogaerts, A.; Carreon, M. L. Ammonia synthesis by radio frequency plasma catalysis: revealing the underlying mechanisms. *ACS Appl. Energy Mater.* **2018**, *1*, 4824–4839.

(17) Murakami, K.; Tanaka, Y.; Sakai, R.; Toko, K.; Ito, K.; Ishikawa, A.; Higo, T.; Yabe, T.; Ogo, S.; Ikeda, M.; et al. The important role of N2H formation energy for low-temperature ammonia synthesis in an electric field. *Catal. Today* **2020**, *351*, 119–124.

(18) Shah, J.; Gorky, F.; Psarras, P.; Seong, B.; Gómez-Gualdrón, D. A.; Carreon, M. L. Enhancement of the Yield of Ammonia by Hydrogen-Sink Effect during Plasma Catalysis. *ChemCatChem 12.4 (2020): 1200-1211*.

(19) Barboun, P. M.; Daemen, L. L.; Waitt, C.; Wu, Z.; Schneider, W. F.; Hicks, J. C. Inelastic Neutron Scattering Observation of Plasma-Promoted Nitrogen Reduction Intermediates on Ni/γ-Al_2 O_3. *ACS Energy Lett.* **2021**, 2048–2053.

(20) Lee, G.; Go, D. B.; O'Brien, C. P. Direct Observation of Plasma-Stimulated Activation of Surface Species Using Multimodal In Situ/Operando Spectroscopy Combining Polarization-Modulation Infrared Reflection-Absorption Spectroscopy, Optical Emission Spectroscopy, and Mass Spectrometry. *ACS Appl. Mater. Interfaces* **2021**, *13*, 56242–56253.

(21) Liu, R.; Hao, Y.; Wang, T.; Wang, L.; Bogaerts, A.; Guo, H.; Yi, Y. Hybrid plasma-thermal system for methane conversion to ethylene and hydrogen. *Chemical Engineering Journal* **2023**, *463*, 142442.

(22) Ndayirinde, C.; Gorbanev, Y.; Ciocarlan, R.-G.; De Meyer, R.; Smets, A.; Vlasov, E.; Bals, S.; Cool, P.; Bogaerts, A. Plasma-catalytic ammonia synthesis: Packed catalysts act as plasma modifiers. *Catal. Today* **2023**, *419*, 114156.

(23) Bayer, B. N.; Bruggeman, P. J.; Bhan, A. Species, Pathways, and Timescales for NH_3 Formation by Low-Temperature Atmospheric Pressure Plasma Catalysis. *ACS Catal.* **2023**, 2619–2630.

(24) Engelmann, Y.; van 't Veer, K.; Gorbanev, Y.; Neyts, E. C.; Schneider, W. F.; Bogaerts, A. Plasma catalysis for ammonia synthesis: A microkinetic modeling study on the contributions of eley–rideal reactions. *ACS Sustain. Chem. Eng.* **2021**, *9*, 13151–13163.

(25) van 't Veer, K.; Engelmann, Y.; Reniers, F.; Bogaerts, A. Plasma-Catalytic Ammonia Synthesis in a DBD Plasma: Role

of Microdischarges and Their Afterglows. *J. Phys. Chem. C* **2020**, *124*, 22871–22883.

(26) Hong, J.; Pancheshnyi, S.; Tam, E.; Lowke, J. J.; Prawer, S.; Murphy, A. B. Kinetic modelling of NH_3 production in N_2 – H_2 non-equilibrium atmospheric-pressure plasma catalysis. *J. Phys. D Appl. Phys.* **2017**, *50*, 154005.

(27) Carrasco, E.; Jiménez-Redondo, M.; Tanarro, I.; Herrero, V. J. Neutral and ion chemistry in low pressure dc plasmas of H2/N2 mixtures: routes for the efficient production of NH3 and NH4(+). *Phys. Chem. Chem. Phys.* **2011**, *13*, 19561–19572.

(28) Matera, S.; Schneider, W. F.; Heyden, A.; Savara, A. Progress in accurate chemical kinetic modeling, simulations, and parameter estimation for heterogeneous catalysis. *ACS Catal.* **2019**.

(29) Ma, H.; Sharma, R. K.; Welzel, S.; van de Sanden, M. C. M.; Tsampas, M. N.; Schneider, W. F. Observation and rationalization of nitrogen oxidation enabled only by coupled plasma and catalyst. *Nat. Commun.* **2022**, *13*, 402.

(30) Schweitzer, B.; Archuleta, C.; Seong, B.; Anderson, R.; Gómez-Gualdrón, D. A. Electronic effects due to organic linker-metal surface interactions: implications on screening of MOF-encapsulated catalysts. *Phys. Chem. Chem. Phys.* **2020**, *22*, 2475–2487.

(31) Bajpai, A.; Frey, K.; Schneider, W. F. Comparison of Coverage-Dependent Binding Energy Models for Mean-Field Microkinetic Rate Predictions. *Langmuir* **2020**, *36*, 465–474.

(32) Wang, S.; Petzold, V.; Tripkovic, V.; Kleis, J.; Howalt, J.; Skúlason, E.; Fernández, E.; Hvolbæk, B.; Jones, G.; Toftelund, A.; et al. Universal transition state scaling relations for hydrogenation and dehydrogenation reactions over transition metals.

(33) Vojvodic, A.; Medford, A. J.; Studt, F.; Abild-Pedersen, F.; Khan, T. S.; Bligaard, T.; Nørskov, J. K. Exploring the limits: A low-pressure, low-temperature Haber–Bosch process. *Chem. Phys. Lett.* **2014**, *598*, 108–112.

(34) Hong, J.; Aramesh, M.; Shimoni, O.; Seo, D. H.; Yick, S.; Greig, A.; Charles, C.; Prawer, S.; Murphy, A. B. Plasma Catalytic Synthesis of Ammonia Using Functionalized-Carbon Coatings in an Atmospheric-Pressure Non-equilibrium Discharge. *Plasma Chem. Plasma Process.* **2016**, *36*, 917–940.

(35) Iwamoto, M.; Akiyama, M.; Aihara, K.; Deguchi, T. Ammonia Synthesis on Wool-Like Au, Pt, Pd, Ag, or Cu Electrode Catalysts in Nonthermal Atmospheric-Pressure Plasma of N_2 and H_2. *ACS Catal.* **2017**, *7*, 6924–6929.

(36) Mao, C.; Li, H.; Gu, H.; Wang, J.; Zou, Y.; Qi, G.; Xu, J.; Deng, F.; Shen, W.; Li, J.; et al. Beyond the Thermal Equilibrium Limit of Ammonia Synthesis with Dual Temperature Zone Catalyst Powered by Solar Light. *Chem* **2019**, *5*, 2702–2717.

(37) Singh, A. R.; Rohr, B. A.; Schwalbe, J. A.; Cargnello, M.; Chan, K.; Jaramillo, T. F.; Chorkendorff, I.; Nørskov, J. K. Electrochemical ammonia synthesis—the selectivity challenge. *ACS Catal.* **2017**, *7*, 706–709.

(38) Back, S.; Jung, Y. On the mechanism of electrochemical ammonia synthesis on the Ru catalyst. *Phys. Chem. Chem. Phys.* **2016**, *18*, 9161–9166.

(39) Shirazi, M.; Bogaerts, A.; Neyts, E. C. A DFT study of H-dissolution into the bulk of a crystalline Ni(111) surface: a chemical identifier for the reaction kinetics. *Phys. Chem. Chem. Phys.* **2017**, *19*, 19150–19158.

(40) Yamijala, S. S. R. K. C.; Nava, G.; Ali, Z. A.; Beretta, D.; Wong, B. M.; Mangolini, L. Harnessing Plasma Environments for Ammonia Catalysis: Mechanistic Insights from Experiments and Large-Scale Ab Initio Molecular Dynamics. *J. Phys. Chem. Lett.* **2020**, *11*, 10469–10475.

(41) Jiang, D. E.; Carter, E. A. Diffusion of interstitial hydrogen into and through bcc Fe from first principles. *Phys. Rev. B* **2004**, *70*, 064102.

(42) Lee, K.; Yuan, M.; Wilcox, J. Understanding Deviations in Hydrogen Solubility Predictions in Transition Metals through First-Principles Calculations. *J. Phys. Chem. C* **2015**, *119*, 19642–19653.

(43) Antunes, R.; Steiner, R.; Romero Muñiz, C.; Soni, K.; Marot, L.; Meyer, E. Plasma-Assisted Catalysis of Ammonia Using Tungsten at Low Pressures: A Parametric Study. *ACS Appl. Energy Mater.* **2021**, *4*, 4385–4394.

(44) Lim, K. H.; Yue, Y.; Bella; Gao, X.; Zhang, T.; Hu, F.; Das, S.; Kawi, S. Sustainable Hydrogen and Ammonia Technologies with Nonthermal Plasma Catalysis: Mechanistic Insights and Technoeconomic Analysis. *ACS Sustain. Chem. Eng.* **2023**.

(45) Psarras, P.; Anderson, R.; Wilcox, J.; Gómez-Gualdrón, D. A. Dissociation, dissolution, and diffusion of nitrogen on v fe and v cr alloy membranes studied by first principles. *J. Phys. Chem. C* **2019**, *123*, 30416–30426.

(46) Psarras, P.; Anderson, R.; Gómez-Gualdrón, D. A.; Wilcox, J. Material Consequences of Hydrogen Dissolution in Palladium Alloys Observed from First Principles. *J. Phys. Chem. C* **2019**, *123*, 22158–22171.

(47) Tanaka, S.; Uyama, H.; Matsumoto, O. Synergistic effects of catalysts and plasmas on the synthesis of ammonia and hydrazine. *Plasma Chem. Plasma Process.* **1994**, *14*, 491–504.

(48) Kim, M.; Biswas, S.; Nava, G.; Wong, B. M.; Mangolini, L. Reduced energy cost of ammonia synthesis via RF plasma pulsing. *ACS Sustain. Chem. Eng.* **2022**, *10*, 15135–15147.

(49) Navascués, P.; Obrero-Pérez, J. M.; Cotrino, J.; González-Elipe, A. R.; Gómez-Ramírez, A. Unraveling Discharge and Surface Mechanisms in Plasma-Assisted Ammonia Reactions. *ACS Sustain. Chem. Eng.* **2020**, *8*, 14855–14866.

SYNOPSIS

The kinetic relevance of radicals in "green," plasma-assisted, catalytic NH_3 synthesis is evinced through microkinetic modeling and experiments.

For Table of Contents Use Only: